Full Length Article

TDERS, an exosome RNA-derived signature predicts prognosis and immunotherapeutic response in clear cell renal cell cancer: a multicohort study

Aimin Jiang [1,#], Ying Liu [1,#], Ziwei He [1,#], Wenqiang Liu [1,#], Qiwei Yang [2,3,#], Yu Fang [1], Baohua Zhu [1], Xiaofeng Wu [1], Huamao Ye [1], Bicheng Ye [4], Shunxiang Gao [5,*], Le Qu [6,*], Wenhao Xu [7,*], Peng Luo [8,*], Linhui Wang [1,*]

[1] *Department of Urology, Changhai Hospital, Naval Medical University (Second Military Medical University), Shanghai, China*
[2] *Department of Urology, Shanghai East Hospital, Tongji University School of Medicine, Shanghai, China*
[3] *Department of Urology, the Third Affiliated Hospital of Naval Military Medical University (Eastern Hepatobiliary Surgery Hospital), Shanghai, China*
[4] *School of Clinical Medicine, Medical College of Yangzhou Polytechnic College, Yangzhou, China*
[5] *Eye Institute and Department of Ophthalmology, Eye & ENT Hospital, Fudan University, Shanghai, China*
[6] *Department of Urology, Affiliated Jinling Hospital, Medical School of Nanjing University, Nanjing, China*
[7] *Department of Urology, Fudan University Shanghai Cancer Center, State Key Laboratory of Genetic Engineering, Collaborative Innovation Center for Genetics and Development, School of Life Sciences, Institute of Biomedical Sciences, and Human Phenome Institute, Fudan University, Shanghai, China*
[8] *Department of Oncology, Zhujiang Hospital, Southern Medical University, Guangzhou, China*

ARTICLE INFO

ABSTRACT

Background: Tumor-derived exosomes are involved in tumor progression and immune invasion and might function as promising noninvasive approaches for clinical management. However, there are few reports on exosom-based markers for predicting the progression and adjuvant therapy response rate among patients with clear cell renal cell carcinoma (ccRCC).

Methods: The signatures differentially expressed in exosomes from tumor and normal tissues from ccRCC patients were correspondingly deregulated in ccRCC tissues. We adopted a two-step strategy, including Lasso and bootstrapping, to construct a novel risk stratification system termed the TDERS (Tumor-Derived Exosome-Related Risk Score). During the testing and validation phases, we leveraged multiple external datasets containing over 2000 RCC cases from eight cohorts and one inhouse cohort to evaluate the accuracy of the TDERS. In addition, enrichment analysis, immune infiltration signatures, mutation landscape and therapy sensitivity between the high and low TDERS groups were compared. Finally, the impact of TDERS on the tumor microenvironment (TME) was also analysed in our single-cell datasets.

Results: TDERS consisted of 12 mRNAs deregulated in both exosomes and tissues from patients with ccRCC. TDERS achieved satisfactory performance in both prognosis and immune checkpoint inhibitor (ICI) response across all ccRCC cohorts and other pathological types, since the average area under the curve (AUC) to predict 5-year overall survival (OS) was larger than 0.8 across the four cohorts. Patients in the TDERS high group were resistant to ICIs, while mercaptopurine might function as a promising agent for those patients. Patients with a high TDERS were characterized by coagulation and hypoxia, which induced hampered tumor antigen presentation and relative resistance to ICIs. In addition, single cells from 12 advanced samples validated this phenomenon since the interaction between dendritic cells and macrophages was limited. Finally, PLOD2, which is highly expressed in fibro- and epi-tissue, could be a potential therapeutic target for ccRCC patients since inhibiting PLOD2 altered the malignant phenotype of ccRCC *in vitro*.

Conclusion: As a novel, non-invasive, and repeatable monitoring tool, the TDERS could work as a robust risk stratification system for patients with ccRCC and precisely inform treatment decisions about ICI therapy.

---

* Corresponding authors.
    E-mail addresses: shunxianggao@163.com (S. Gao), septsoul@smmu.edu.cn (L. Qu), xwhao0407@fudan.edu.cn (W. Xu), luopeng@smu.edu.cn (P. Luo), wanglinhui@smmu.edu.cn (L. Wang).
    # These authors contributed equally to this work.

1. Introduction

Renal cell carcinoma (RCC) remains a significant health concern with its high prevalence and detrimental impact on the genitourinary system.[1] In line with recent global cancer statistics, the escalating numbers are disconcerting, presenting over 400,000 fresh cases of RCC and an excess of 180,000 fatalities occurring worldwide.[2] Among the diverse subtypes encompassing RCC, clear cell RCC (ccRCC) emerges as the prevailing variant, constituting nearly 70% of all diagnosed cases.[3] Regrettably, ccRCC often presents with no symptoms or nonspecific symptoms, which results in one-third of cases being diagnosed at an advanced stage or after metastasis has occurred. Consequently, the prognosis for patients with advanced ccRCC is extremely poor, with a meager 12% survival rate over a 5-year period.[4] Currently, the postoperative detection of RCC primarily relies on imaging techniques such as computed tomography (CT), enhanced CT, and whole-body bone scans.[5] However, these methods have limitations, including high radiation doses and costs, which pose challenges for clinicians. Additionally, while targeted therapy, immune therapy, and combined therapies have shown some promise in extending the survival time of patients with locally advanced or metastatic disease, only a small subset of patients actually derive any benefit from these approaches.[6,7] Hence, it is of utmost importance to explore alternative approaches that are convenient, repeatable, robust, economical, and noninvasive to improve the prognosis of ccRCC. The development of effective models is crucial for accurately stratifying the risk and making targeted therapy a more viable option for patients.

Exosomes are small extracellular vesicles that originate from endosomes, measuring 30–150 nm in size. They contain a variety of components, including proteins, nucleic acids, lipids, and metabolites.[8,9] These vesicles play a pivotal role in facilitating communication between cells, both in normal physiological conditions and in pathological states.[10] Notably, tumors have been observed to release a large quantity of exosomes. Compared to individuals without cancer, cancer patients exhibit higher levels of exosomes in their plasma or other bodily fluids. Mounting evidence indicated that exosomes derived from tumor have a significant impact on various processes associated with tumorigenesis, such as tumor invasion, metastasis, and resistance to treatment.[11] Upon uptake by immune cells and stromal cells within the tumor microenvironment, these exosomes induce alterations in cell behavior and infiltration patterns.[12] This unique cargo carried by exosomes, their abundance in peripheral circulation, and the ease of liquid biopsy make them valuable as cancer biomarkers.[13] Previous studies have demonstrated that exosomes derived from RCC contribute to the formation of premetastatic niches, angiogenesis, drug resistance, and immune evasion.[14] These activities ultimately influence the overall survival time of RCC patients. For instance, our own research has identified a long noncoding RNA called lnc*ARSR*, which acts as an exosome-transmitted molecule promoting sunitinib resistance in RCC.[15] Recent studies have demonstrated the significant involvement of exosomes in facilitating intercellular communication and promoting the progression and distant metastasis of RCC. Exosomes have emerged as a promising biomarker for the early detection and therapeutic management of tumors. Nevertheless, the precise prognostic value of exosomes in RCC prognosis remains to be elucidated.

In this study, we conducted an extensive investigation into the mRNA cargo carried by exosomes isolated from plasma samples of patients diagnosed with ccRCC. Remarkably, we found that these exosomal mRNA profiles exhibited similar deregulation patterns as observed in the corresponding tumor tissues. Leveraging advanced computational techniques such as the Lasso and bootstrap algorithms, we devised a novel signature, denoted as the TDERS. The primary objective was to utilize TDERS to predict overall survival outcomes across three distinct pathological subtypes of RCC. Furthermore, we explored the potential of TDERS as a predictive tool for immune checkpoint blockade therapies, while concurrently deciphering the association between high TDERS levels and an immunosuppressive microenvironment. Additionally, through inte-

gration with drug sensitivity and genomic datasets, we investigated underlying mechanisms linked to TDERS.

2. Materials and methods

2.1. Dataset collection and processing

To reveal the prognostic impact of the exosome-derived signature in RCC patients, more than 2000 RCC cases with tumor sample-derived expression profiles, including cohorts TCGA-KIRC ($n = 530$), TCGA-KIRP ($n = 288$), TCGA-KICH ($n = 65$), JAPAN-KIRC ($n = 100$), ICGC-EU ($n = 91$), GSE22541 ($n = 40$), Motzer's cohort ($n = 823$), Branu's cohort ($n = 311$) and our inhouse cohort ($n = 84$), were adopted in this work.[16–18] All the baseline information and characteristics of the above cohorts were summarized in Supplementary Table 1. In addition, genomic mutation and copy number variation (CNV) information of RCC were downloaded from the GDC portal. For microarray data retrieved from the Gene Expression Omnibus (GEO), the samples were downloaded by the R package GEOquery and log2-transformed.[19] Raw counts were adjusted for gene length using transcript-per-million (TPM) normalization, and subsequently log2-transformed. The exclusion criteria were as follows: (1) patients were not diagnosed with RCC; (2) patients lacked corresponding sequence and clinical outcome information; and (3) died within 30 days after diagnosed with RCC.

2.2. Sing-cell RNA sequencing and analysis pipeline

Six paired ccRCC samples, consisting of tumor and normal tissues, were collected from our institution. The single-cell RNA sequencing (scRNA-seq) samples were processed immediately after the removal of fresh tissues. All patients had clear-cell histology and had not undergone any therapy prior to surgery. Single-cell extraction and 10X droplet-based sequencing were conducted following the manufacturer's instructions and our previous protocols. Data quality control was performed using Seurat (version 3.0.1). Cells with fewer than 200 or more than 5000 genes, or with over 30% mitochondrial genes, were classified as low-quality and subsequently excluded. Doublet identification and removal were carried out using the DoubletFinder package (version 2.0.3). The 2000 highly variable genes (HVGs) were identified through the "FindVariableGenes" function. Principal component analysis (PCA) was conducted on the single-cell expression matrix utilizing the RunPCA function, with the top 30 principal components utilized for clustering via the Louvain graph-clustering method. Subsequently, batch-effect correction was performed for each sample using the RunHarmony method. Markers for each primary cell cluster were identified using the FindAllMarker function. Cell type markers were sourced from the CellMarker website and previous research studies. Differential gene expression analysis was conducted using the Seurat function, with a significance threshold of $P < 0.05$ for identifying differentially expressed genes (DEGs). The R package CellChat was utilized for analyzing and visualizing cell interactions (version 1.6.1).

2.3. Establishment of an exosomal-derived risk score system

Three steps were introduced to identify and construct the risk score system, and the details were as follows: first, DEG between exosomes from ccRCC and normal tissues were extracted in our previous study, and the interaction between those DEG and corresponding DEG from bulk sequences (tumor *vs.* normal tissues) were extracted. Next, the interacting DEGs were filtered after prognostic analysis in both TCGA-KIRC and E-MTAB-1980. Finally, those DEGs from both exosomes and bulk were enrolled to perform Lasso-Cox (alpha = 1, nfolds = 10, xvar = lambda) and bootstrap (statistic = rsq, R = 1000) analysis. Finally, 12 mRNAs (*COBLL1, PLOD2, MEGF9, EMCN, PLXNA2, ASRGL1, MICU1, TTC33, WDR11, UPB1, SLC5A12, LSM14A*) were identified to be statistically prognosis relevant among RCC. To prevent the interference

of sequencing data depth and platform technology, we calculated the risk score based on the expression standard deviation to calculate the risk coefficient. The hazard ratio (HR) and corresponding standard error (SE) of HR for each of the 12 exosome-derived signatures determined their weight in the risk score system. HR of each gene was calculated by function of "coxph" form R package survival. Simplistically, the risk score was calculated as follows:

$$TDERSE = \sum_{i=1}^{12} \left(\frac{HRi - 1}{SEi * HRi} * Gi \right)$$

where Gi is the abundance of gene i in each RCC sample, and SEi represents SE of each gene. Thus, RCC samples from each cohort were divided into two subtypes, high and low subtypes, based on the median value of the risk score. Finally, we defined this risk score as TDERS.

2.4. Multiomics landscape between high- and low- TDERS groups

Prior to conducting any comparisons, genes exhibiting fewer than 10 total reads across all samples were excluded. We employed DESeq2 (version 1.42.0), utilizing its standard settings to carry out differential expression analysis through approaches reliant on the negative binomial distribution.[20] This analysis modeled the read counts according to negative binomial distributions, which incorporated both estimated means and gene-specific dispersion parameters. Each gene's data was then fit into a generalized linear model framework. For assessing statistical significance and adjusting for multiple testing, we applied Wald statistics along with the Benjamini and Hochberg correction method. Subsequently, DEG meeting the significance criteria (adjusted P value < 0.05) were selected for further analysis. To account for multiple testing, the Benjamini-Hochberg correction was applied to calculate adjusted P values. DEG identification (thresholds set at adjusted P value < 0.01, log fold change > 2), as well as corresponding annotation analysis, was conducted using R packages Deseq2 and ClusterProfiler (version 4.10.0).[21] Annotation files sourced from the Molecular Signature Database (MSigDB) were utilized.[22] Mutation landscape analysis of TCGA-KIRC was carried out, and visualizations were generated using the Maftools (version 2.18.0) and ggplot2 R (version 3.3.3) packages.[23] The study utilized single-sample gene set enrichment analysis (ssGSEA) from the R package GSVA (version 1.50.0) to assess the relative infiltration of 28 immune cells in the TCGA-KIRC cohort.[24] Additionally, six alternative algorithms, including TIMER, quanTIseq (version1.10.0), MCP-counter (1.2.0), xCell (1.1.0), EPIC (version 1.1.5), and ESTIMATE (1.0.13), were employed to validate the consistency and reliability of the ssGSEA findings. The tumor mutation burden (TMB) score of ccRCC samples was quantified using a classical algorithm embedded in maftools. CNV information, including copy number loss and gain frequency, was obtained from the Genepattern website by uploading CNV data and utilizing the GISTIC module.[25] For drug sensitivity analysis, the Genomics of Drug Sensitivity in Cancer (GDSC) and CMap databases, along with the oncoPredict (1.1.0) R package, were employed to examine the correlation between the risk score and half maximal inhibitory concentration (IC50) values. Additionally, the Tumor Immune Dysfunction and Exclusion (TIDE) algorithm was used to predict the response to immunotherapy in both TDERS high and low groups.[26]

2.5. Cell culture and in-vitro experiments

RCC cell lines (786-O and OSRC2) were utilized in this research. These cell lines were purchase from reputable sources, including the American Type Culture Collection (ATCC, Manassas, VA, United States) and the National Infrastructure of Cell Line Resource (Beijing, China). To maintain their viability, the cell lines were regularly cultured in RPMI 1640 or DMEM supplemented with 10% fetal bovine serum from Invitrogen (Carlsbad, CA, United States). The incubation process was performed at a temperature of 37 °C in an environment containing 5% CO_2. For the purposes of this study, PLOD2 shRNA was procured

from GeneChem Corporation (Shanghai, China). To assess the impact of PLOD1 on proliferation and motility in ccRCC, CCK8 and wound healing assays were employed. In 96-well plates, each well was seeded with 2×10^3 cells. The cells were then treated with CCK8 (YEASEN, China) at 0, 24, 48, 72, and 96 h as per the manufacturer's instructions. The treated cells were subsequently subjected to absorbance measurements at 450 nm using a NanoDrop 2000 spectrophotometer (NanoDrop Technologies, USA). In the case of wound healing assay, $2-3 \times 10^6$ cells were plated in each well of a six-well plate and transfected with vectors for a period of 24 h. The cell layers were gently scratched using sterile tips before being washed with PBS. Following an additional incubation of 0 and 24 h, images were captured. The aforementioned assays were performed in triplicate. Transwell assays were conducted using chambers from Corning, with some receiving a Matrigel coating to assess the invasive potential of ccRCC cell lines. Specifically, ccRCC lines 786-O and OSRC2 were cultured in six-well plates for 48 h before being dissociated with 0.25% trypsin and subsequently suspended in serum-free medium. For invasion assays, 2×10^5 cells in 200 μL were seeded into each Matrigel-precoated upper chamber of the Transwell. The lower chamber was filled with 500 μL of complete medium containing 10% fetal bovine serum (FBS) to serve as a chemoattractant. After 24 h, non-invading cells were gently removed from the upper membrane with a cotton swab. Cells that had migrated to the lower surface were fixed with 4% paraformaldehyde, stained with 0.5% crystal violet, and quantified. Photographic documentation of the results was performed using an Olympus microscope, facilitating a detailed analysis of the metastatic properties of these cell lines.

2.6. Statistical analysis

All datasets, encompassing both transcriptome and genomic information, were processed and analyzed using R software (version 4.2.0) and SPSS. To compare differences in continuous and quantitative variables, a combination of Kruskal–Wallis, *t*-tests, and chi-square tests was employed as appropriate. Continuous numerical variables were presented as mean ± standard deviation (SD). Statistical significance among variables was assessed using Student's *t*-test and two-tailed Wilcoxon test. Spearman correlations were calculated between the risk score and continuous variables specific to RCC using the R package corrplot (version 0.92). Correlations among various variables were visualized using the corrplot package. Kaplan-Meier curves and time receiver operating characteristic (ROC) curves were generated using the R packages survival and pROC (version 1.18.0), respectively. A P value less than 0.05 indicated statistical significance. For further details regarding bioinformatics analyses, refer to previous studies.[27–30]

3. Results

3.1. Construction of a risk model based on exosome-derived signatures

The workflow of our study is illustrated in Fig. 1. In our previous research, our team developed a liquid biopsy diagnostic model using exosomes for the early diagnosis and prognosis evaluation of ccRCC. This model demonstrated excellent performance in distinguishing ccRCC from benign renal masses. We analyzed the exosome sequencing datasets and identified 210 DEG (Supplementary Table 2). We then investigated the prognostic value of these genes in the ccRCC cohort. Initially, we combined the DEGs from exosome sequences and DEG between tumor and normal tissues from the TCGA-KIRC dataset to construct a prognostic model (Supplementary Fig. 1A). Those DEG were annotated in amino acid metabolic and pantothenate and CoA biosynthesis (Supplementary Fig. 1B). Subsequently, we selected DEGs that could predict OS with AUCs greater than 0.55 in both TCGA-KIRC and JAPAN-KIRC cohorts to construct the risk system (Fig. 2A and B). Interestingly, we found that a well-known ccRCC-related gene, VHL, was among these genes. To refine the model parameters, we applied least
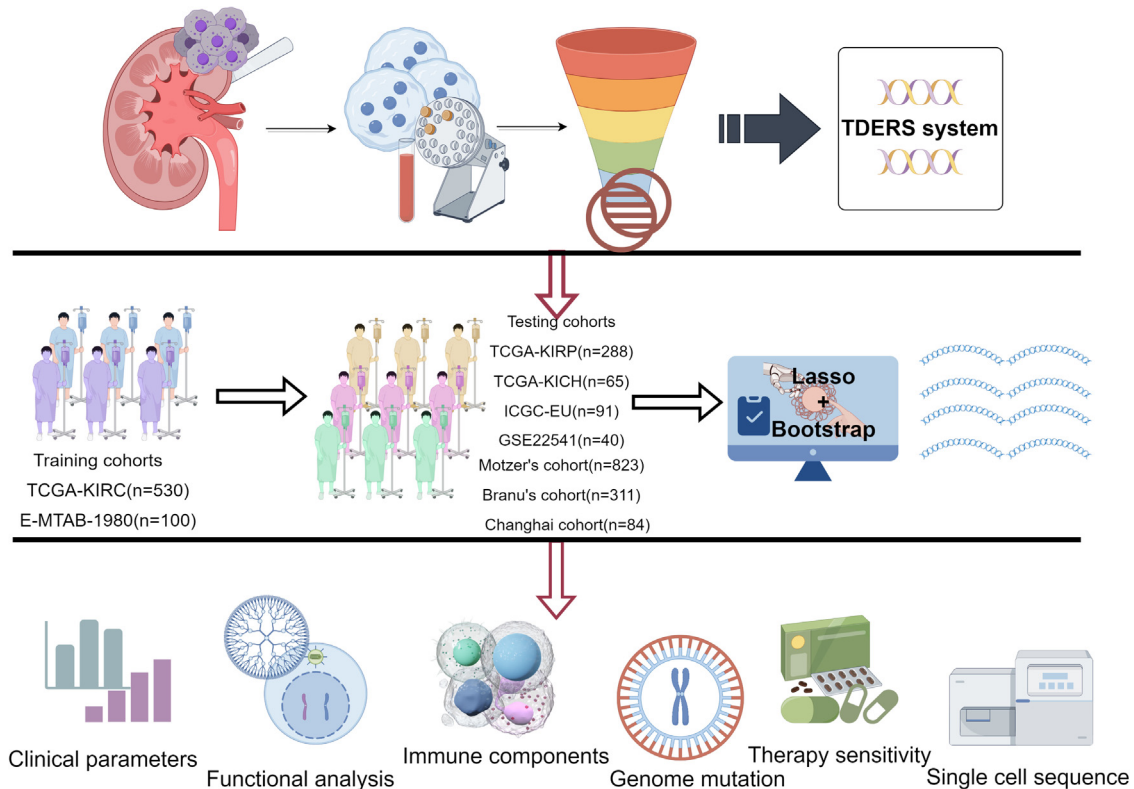
Fig. 1. A flowchart depicting a comprehensive analysis of TDERS (Tumor-Derived Exosome-Related Signatures) in postoperative cohorts with renal cell carcinoma.

absolute shrinkage and selection operator (Lasso) Cox regression and bootstrapping to identify the most important genes highly predictive of OS. Ultimately, we identified twelve genes (*COBLL1, PLOD2, MEGF9, EMCN, PLXNA2, ASRGL1, MICU1, TTC33, WDR11, UPB1, SLC5A12*, and *LSM14A*) with a lambda value of 0.008 (Fig. 2**C**). Considering the biological characteristics of these genes, we named this risk score system TDERS (Tumor-derived Exosome-Related Risk Score). Notably, *PLOD2* was highly expressed in the TDERS high group, while the other genes exhibited relatively higher expression in the TDERS low group (Supplementary Fig. 2A).

In the TCGA-KIRC cohort, patients in the TDERS high group had significantly poorer OS (OS, $P < 0.01$), progression-free survival (PFS, $P < 0.01$), and disease-specific survival (DSS, $P < 0.01$) compared to those with lower risk scores (Fig. 2C, Supplementary Table 3). Moreover, we observed satisfactory AUC scores in the TCGA-KIRC cohort, with values of 0.73, 0.7, 0.71, and 0.72 at 1 year, 2 years, 3 years, and 5 years, respectively (Fig. 2D). To assess the predictive accuracy of the model, we utilized calibration curves to estimate the accuracy of the risk score system in predicting patient prognosis. As depicted in Fig. 2E, our risk score system performed well in predicting patient prognosis at 1 year, 2 years, 3 years, and 5 years of OS. To address the practical requirements of clinical decision-making, we employed decision curve analysis (DCA) to evaluate the net benefit rate of our model. As expected, both the prognostic model and tumor staging achieved high net yields, with our risk score model demonstrating superior performance in predicting OS, particularly at the 5-year OS (Fig. 2F and Supplementary Fig. 2B).

3.2. Validation of TDERS among external datasets

To evaluate the accuracy and generalizability of the TDERS, we conducted validation analyses using multiple external cohorts comprising ccRCC and two pathological cohorts of RCC, namely JAPAN-KIRC, TCGA-KIRP, TCGA-KICH, and GSE22541. As depicted in Fig. 3A, the

TDERS high group consistently exhibited poorer prognosis compared to the TDERS low group across all RCC cohorts ($P < 0.001$). Remarkably, in all external datasets, the majority of AUC values for model prediction exceeded 0.7 (Fig. 3B). Notably, the model demonstrated an exceptional prediction AUC of 0.98 for 1-year and 2-year survival in KICH patients (Fig. 3B). Calibration curve analysis revealed that the model exhibited favorable predictive accuracy for 3-year and 5-year survival in RCC patients, with minimal deviation from observed survival rates (Fig. 3C). Consistent with the findings in TCGA-KIRC, DCA demonstrated that the TDERS risk model offered higher net benefits at lower threshold probabilities in JAPAN-KIRC, TCGA-KIRP, and TCGA-KICH cohorts, particularly for 5-year OS (Fig. 3D). Furthermore, when applied to the ICGC-EU cohort, the TDERS system demonstrated robust performance, as indicated by results shown in Supplementary Fig. 3A-D.

3.3. TDERS performed well among patients treated with immune checkpoint inhibitor

The combination of atezolizumab and bevacizumab has demonstrated clinical activity in patients with advanced RCC.[31] However, due to tumor heterogeneity, only a small proportion of advanced RCC patients are likely to benefit from immune checkpoint inhibitor (ICI). Therefore, we aimed to assess the predictive performance of TDERS in determining the effectiveness of ICI therapy, using the cohorts from Motzer and Branu. In both the Motzer and Branu cohorts, patients with high-risk scores based on TDERS showed poorer prognosis compared to those with low-risk scores ($P < 0.001$). The model exhibited high accuracy, as indicated by the high AUC in both cohorts (Supplementary Fig. 4A). Surprisingly, the predicted AUCs for the 2-year and 3-year OS rates in the Checkmate cohort were remarkably high, at 0.95 and 0.91, respectively (Supplementary Fig. 4B). Calibration plots demonstrated a better fit between the predicted survival probabilities and the actual survival rates for the 1-year time point (Supplementary Fig. 4C). Furthermore, by employing DCA, we compared the advantages and disadvantages of
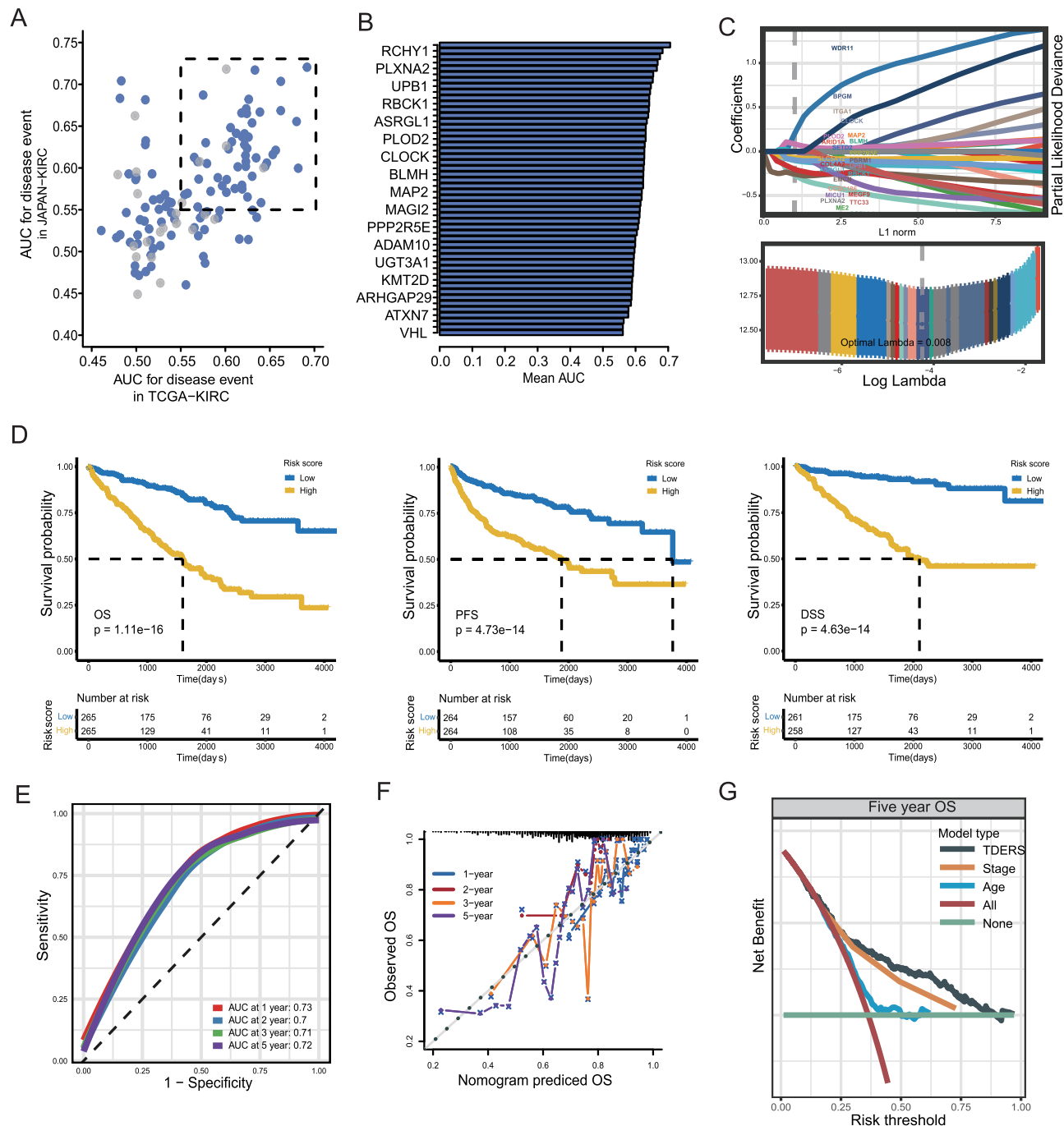
Fig. 2. The construction of TDERS is based on exosome-derived molecules. (A) The prognostic value of candidate genes involved in overall survival (OS) is evaluated using the AUC in the TCGA and JAPAN-KIRC datasets. Genes with no detectable protein expression in renal cancer from Clinical Proteomic Tumor Analysis Consortium were excluded and are colored in gray. (B) The importance of genes involved in the integration datasets of TCGA-KIRC and JAPAN-KIRC is ranked using a bar plot. (C) LASSO coefficients produced by LASSO regression analysis (up) and Lasso coefficient profiles of candidate genes (down). (D) Survival analysis of two risk groups based on OS, PFS, and DSS. (E) The risk model demonstrates satisfactory AUC scores in the TCGA-KIRC cohort. (F) The accuracy of the risk model is evaluated using the calibration curve, where a slope closer to 1 indicates higher prediction accuracy. (G) Decision curve analysis curves compare TDERS, stage, and age in predicting 5-year OS in TCGA-KIRC. AUC, area under the curve; DSS, disease-specific survival; OS, overall survival; PFS, progression-free survival.

TDERS with the IMDC and MSKCC models. The TDERS model showed slightly better performance than the IMDC and MSKCC models (Supplementary Fig. 4D). In Motzer's cohort of 823 RCC patients, the TDERS effectively predicted the prognosis of patients receiving atezolizumab plus bevacizumab and sunitinib treatment, with AUCs of 0.62 and 0.71, respectively (Supplementary Fig. 4E). Additionally, in our in-house cohort, consisting of 94 advanced RCC samples and 8 patients who received ICI, the TDERS was able to accurately predict survival outcomes.

The low-risk TDERS group exhibited longer overall survival compared to the high-risk TDERS group (Supplementary Fig. 5A), and the average AUCs at 1-, 2-, 3-, and 5- year were consistently above 0.65 (Supplementary Fig. 5B). The calibration plot and DCA further demonstrated the efficacy of the TDERS in our in-house cohort (Supplementary Fig. 5C and D). Notably, the imaging analysis revealed a strong correlation between the TDERS and the efficacy of immunotherapy (Supplementary Fig. 5E). In order to assess the efficacy of the TDERS system in
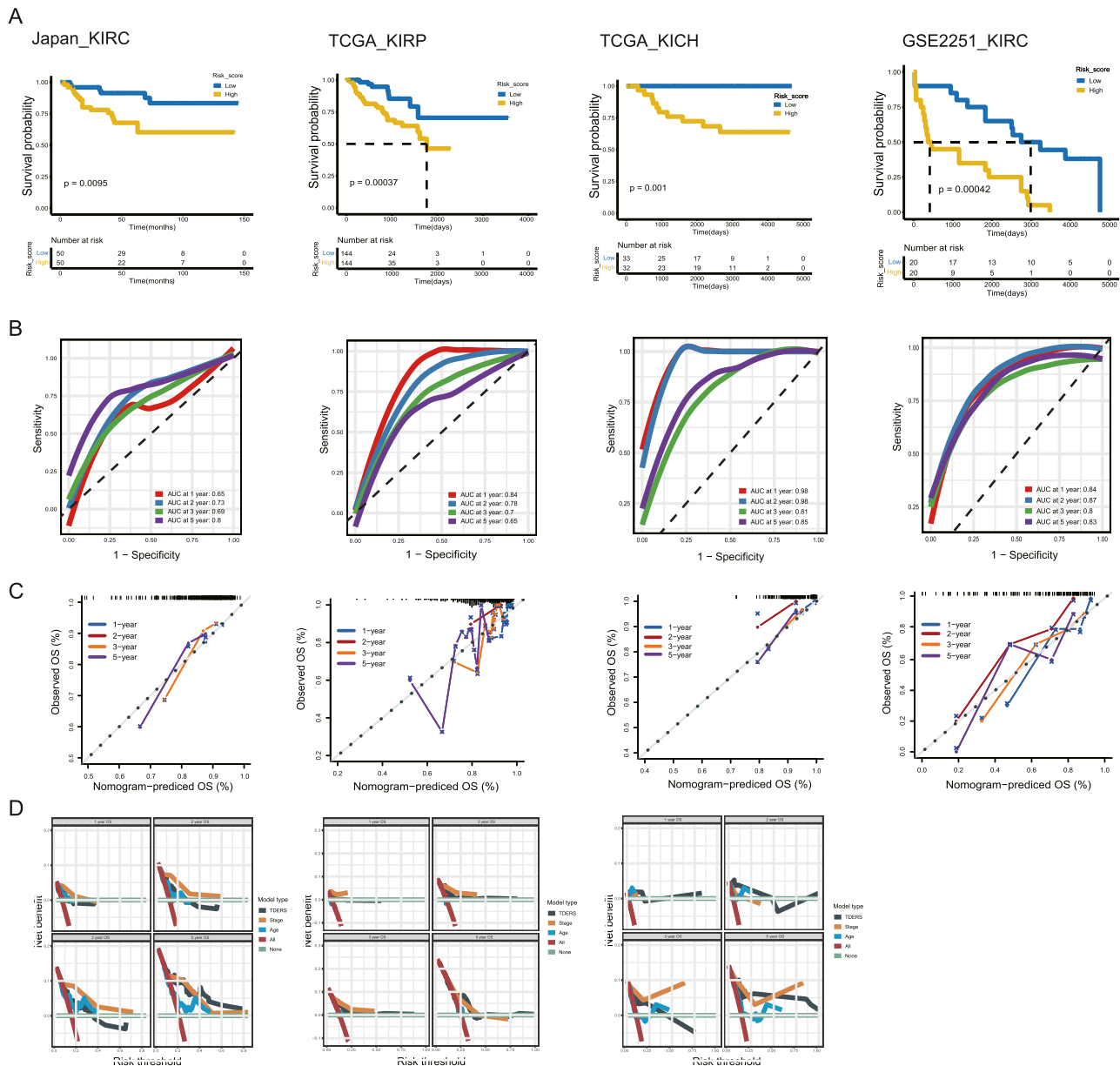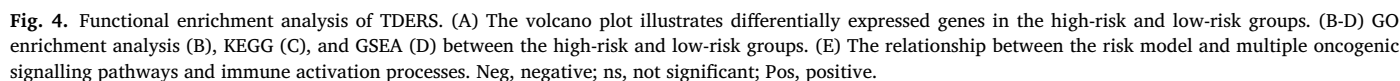
Fig. 3. Validation of TDERS using external datasets. (A) Kaplan-Meier plot demonstrates distinctive prognosis of OS in the JAPAN-KIRC, TCGA-KIRP, TCGA-KICH, and GSE22541 cohorts. (B) The risk model shows satisfactory AUC scores in these four datasets. (C) The accuracy of the risk model is evaluated using the calibration curve. (D) Decision curve analysis compares multiple prognostic models in terms of net benefit in these four datasets. AUC, area under the curve; OS, overall survival.

relation to other signatures, a comprehensive review of published signatures was conducted. Univariate Cox regression analysis was performed on all datasets for each signature, revealing that only the TDERS model exhibited a statistically significant association with prognosis across all cohorts (Supplementary Fig. 6).

3.4. Cornification, hypoxia, coagulation and hampered APM were activated in the TDERS high group

To better understand the biological differences resulting in distinct clinical outcomes between the high and low TDERS groups, we performed functional enrichment analysis of the DEGs derived from the two groups. The volcano plot in Fig. 4A demonstrates the detailed DEG information. GO enrichment analysis showed that the DEGs were mainly enriched in cornification, antibacterial humoral response, keratinization, and acute phase response (Fig. 4B). GSVA hinted that the

TDERS high group was activated in KRAS, hypoxia, myogenesis, peroxisome and coagulation, whereas the TDERS low group was activated in heme metabolism, PI3K-AKT-MTOR signaling, mitotic spindle and G2M checkpoint (Fig. 4C). GSEA indicated that DEGs were mainly concentrated in immune-related pathways in IL-17, cytokine–cytokine receptor interaction, complement and coagulation cascades, fatty acid degradation, collection duct acid secretion and citrate cycle (Fig. 4D). More importantly, when the TDERS was correlated with the antitumour-related immune score and immune circle (Fig. 4E), obvious negative relationships were observed between the TDERS and tumor antigen presentation-related signals and cancer immunity cycle, including cancer antigen presentation, Th22 cell recruiting, monocyte recruiting and Treg cell recruiting. All these findings indicated that the TDERS was significantly correlated with anti-immune processes, which inspired us to investigate the detailed immune infiltration differences and ICI responses between the TDERS high and low groups.

Fig. 4. Functional enrichment analysis of TDERS. (A) The volcano plot illustrates differentially expressed genes in the high-risk and low-risk groups. (B-D) GO enrichment analysis (B), KEGG (C), and GSEA (D) between the high-risk and low-risk groups. (E) The relationship between the risk model and multiple oncogenic signalling pathways and immune activation processes. Neg, negative; ns, not significant; Pos, positive.

3.5. Distinctive immune profiles and therapy heterogeneity between different TDERS groups

Immunotherapy has gradually become the first-line treatment for advanced RCC and has achieved satisfactory results. In the intricate landscape of RCC, the tumor microenvironment is characterized by a rich infiltration of immune and stromal cells. This complex interplay of cel-

lular constituents plays a pivotal role in the oncogenesis and progression of RCC. To compare the differences in immune infiltration patterns between the high and low TDERS groups, specific immune components and immune steps were analyzed. Generally, the TDERS low group was activated in the tumor immune microenvironment and lymphocytes, since most immune cells, including CD8 T, activated natural killer (NK), activated CD4 memory cell and dendritic cells; which only resting NK and
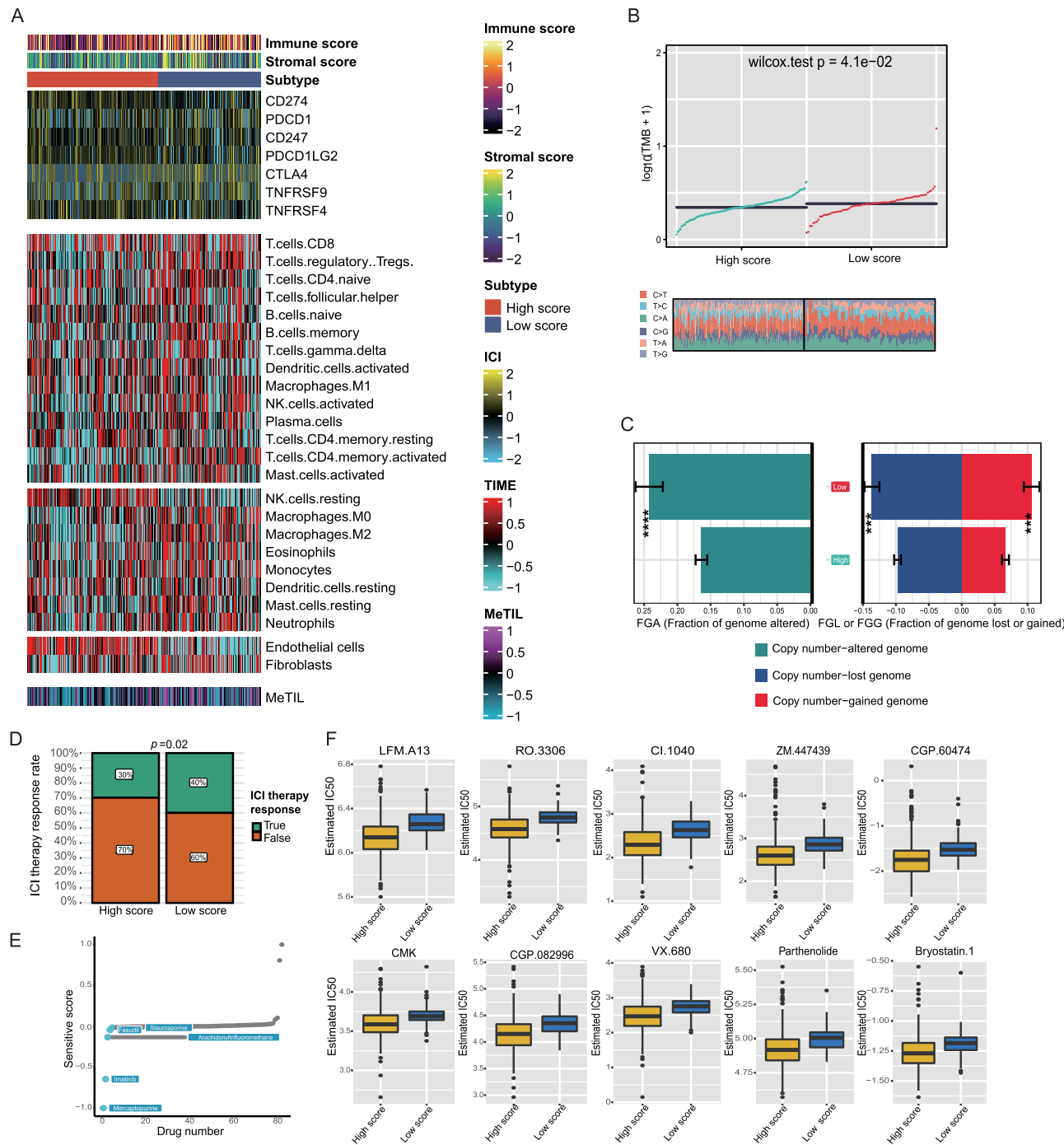
Fig. 5. Correlation between immune infiltration profiles, related targets, and TDERS. (A) Heatmap indicates different immune infiltrate features between the two groups. (B) Tumor mutation burden is compared between the two groups. (C) Copy number variations are compared between the two groups. (D) Predicted immunotherapy responses are compared between the two subgroups. (E) Targeted drugs predicted for the high-risk group. (F) Novel molecular agents identified for the high-risk group from the Genomics of Drug Sensitivity in Cancer database.

endothelial cell were relatively enriched in TDERS high group (Fig. 5A). In addition, the low-risk group was marked with a greater TMB and a higher proportion of CNV (Fig. 5B and C). This high mutational burden and CNV in the TDERS low group may lead to better responsiveness to immunotherapy (Fig. 5D). In addition, when inferring the detailed mutation landscape, we noticed that the leading mutated genes in the TDERS low group were *VHL* (47%), *PBRM1* (32%), *TTN* (22%) and *SETD2* (15%), while the landscape in the TDERS high group was *PBRM1* (53%), *VHL* (52%) and *TTN* (13%) (Supplementary Fig. 7A). In addition, mutation events of *PBRM1, DYNC1H1, MAGEC1, MLLT4, ROCK1* and

CSMD1 were protective in the TDER high group (Supplementary Fig. 7B). Given the recently reported evidence indicating a strong correlation between a high burden of copy number loss and resistance to anti-CTLA-4 blockade, our next objective was to investigate copy number alterations between the low and high TDERS groups.[32,33] Consistently, patients in the high TDERS group had a lower burden of gain and loss at the focal level, as well as a lower burden of gain at the arm level compared to those in the low TDERS group (Supplementary Fig. 7C). Furthermore, the TDERS low group exhibited significantly higher frequencies of arm-level amplification and deletion than the TDERS high group
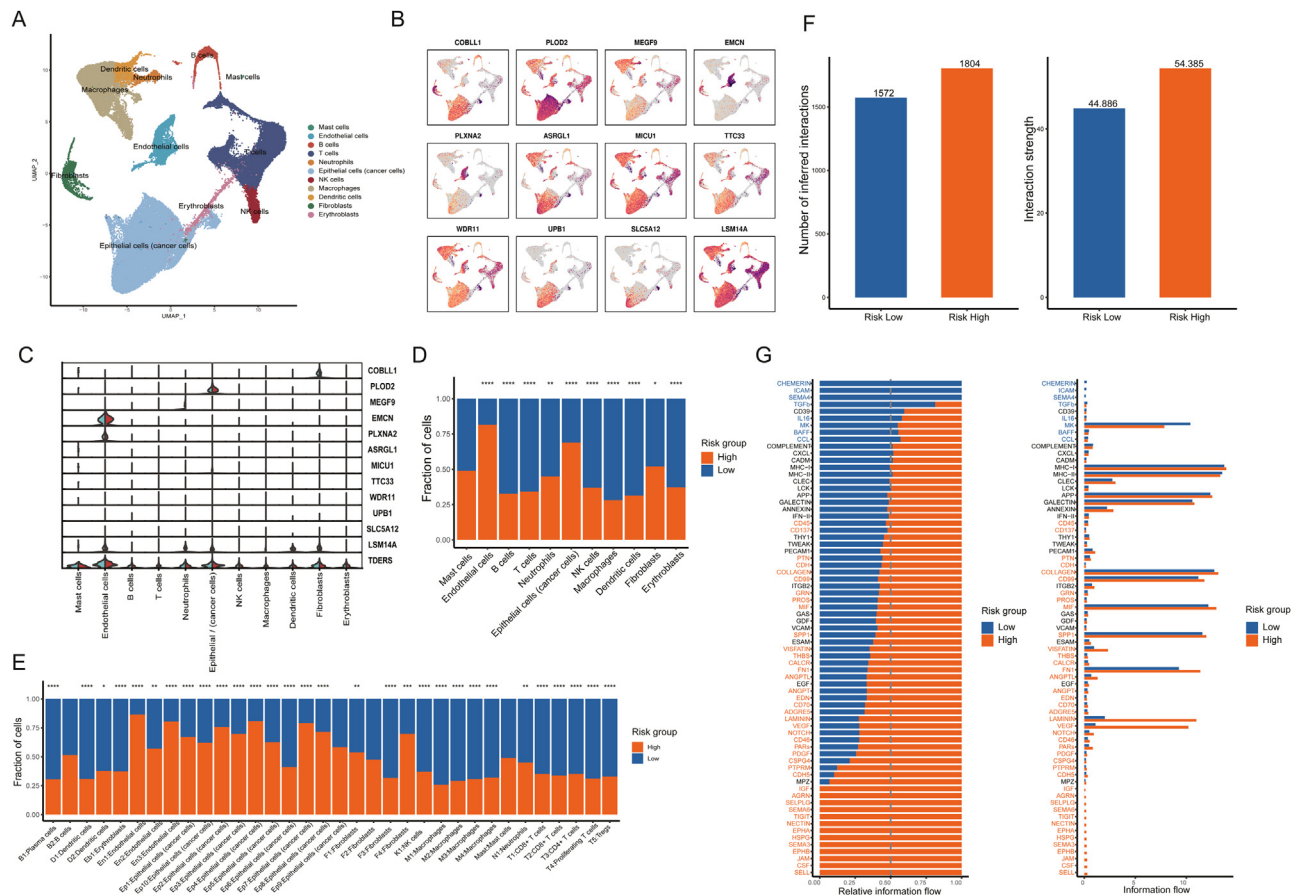
Fig. 6. The role of TDERS at the single-cell level. (A) UMAP plot showing 13 clear cell renal cell carcinoma cell types. (B, C) UMAP plot (B) and violin plot (C) showing the expression of genes comprising TDERS. (D, E) Bar graph indicating the frequency of representative cell clusters in the high-risk and low-risk groups of TDERS. (F) Bar graph showing the frequency of cell communication in the high-risk and low-risk groups. (G) Different cell communication signals observed between the high-risk and low-risk groups of TDERS. UMAP, uniform manifold approximation and projection.

($P < 0.001$) (Supplementary Fig. 7D). To identify potential clinical targeted drugs, we utilized therapy information from the Cmap database. Our screening yielded several candidates, namely fasudil, staurosporine, imatinib, and mercaptopurine, which showed promise for the TDERS high group (Fig. 5E). Additionally, we analyzed the GDSC database to explore other potential drugs. The results indicated that the TDERS high group might exhibit sensitivity to LFM, as well as A13, RO.3306, CI.1040, ZM.447439, and CGP.60474 (Fig. 5F). However, it is important to note that further *in vivo* and *in vitro* studies are necessary to validate the therapeutic efficacy of these agents.

3.6. Single-cell analysis of TDERS in ccRCC

However, there are limitations to bulk RNA sequencing due to its characteristics. In this method, the expression level of a gene is calculated by taking the mean value of all cells in the tissue. To overcome this limitation, we performed single-cell RNA sequencing on three samples of ccRCC. Our analysis involved examining over 60,000 cells, which were then classified into 11 clusters based on classic cell markers. These clusters included mast cells, endothelial cells, B cells, T cells, neutrophils, epithelial cells, natural killer cells, macrophages, dendritic cells, fibroblasts, and erythroblasts (Fig. 6A). In our scRNA analysis, we discovered that 12 genes, specifically the TDERS gene group, showed differential expression among different cell types. Furthermore, most genes within this group displayed relatively low expression levels, which can be attributed to the sequencing depth of scRNA (Fig. 6B). Aligning with these results, we found that the gene *PLOD2* was highly expressed in ccRCC

tumor cells, while TEDRS exhibited high expression in both endothelial cells and tumor cells (Fig. 6C). Upon dividing all cells into two groups - TEDRS high and low - using the median level of TDERS, we observed variations in the cell proportion between these groups. Specifically, the TDERS low group exhibited a higher proportion of endothelial cells, epithelial cells, and fibroblasts, while immune components such as B cells, T cells, NK cells, macrophages, and erythroblasts were relatively low in this group (Fig. 6D). Notably, these findings remained consistent when further categorizing all cell types into minor groups (Fig. 6E).

Different cell proportions might be explained by distinct signal transport patterns; thus, we performed a cell communication or interaction analysis between the TDERS high and low groups. Obviously, the total interaction number and strength of the TDERS high group were more frequent than those of the low group (Fig. 6F). Notably, we found that the communication frequency between endothelial cells and the remaining cell types, including endothelial, epithelial, and fibroblasts, was high, while tumor antigen presentation-related interactions between macrophages and dendritic and B cells were inhibited in the TDERS high group (Supplementary Fig. 8A and B). Aided by inner signals from the CellChat package, we noticed that both incoming and outgoing signal patterns of laminin and VEGF were high in the high-risk group (Supplementary Fig. 8C). Since T-cell activation is involved in immunity, we next compared the interaction of T cells and the remaining cell types and found that the interaction strength of ADGRE5-CD55 between T cells and neutrophils was aberrantly high in the TDERS high group (Supplementary Fig. 8D). Finally, we found that some signatures were conserved in the TDERS high group, including *SELL*, CSF, *JAM, EPHB,*
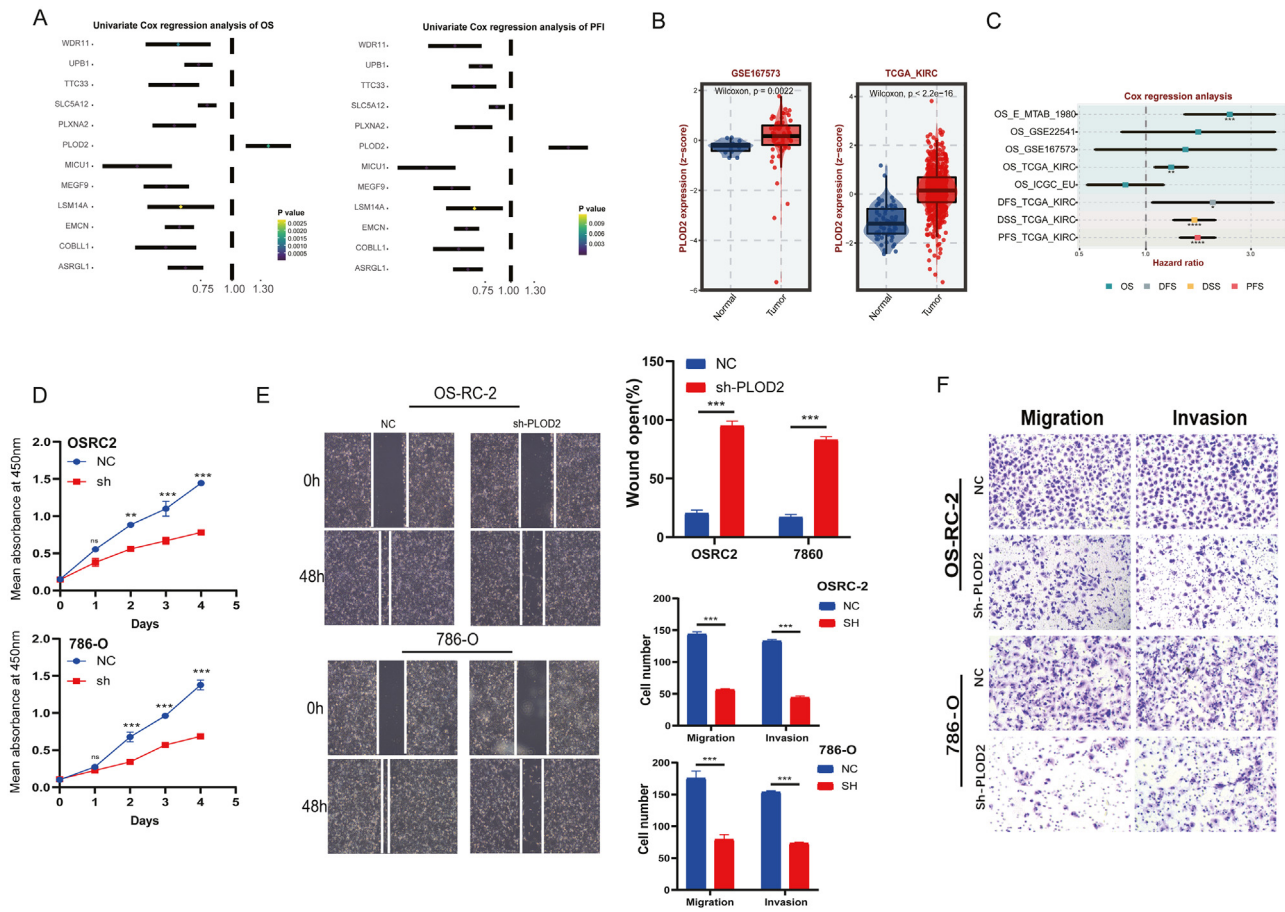
Fig. 7. Clinical and biological roles of PLOD2 in ccRCC. (A) Hazard ratios of 12 TDERS genes for OS and PFI in TCGA-KIRC. (B) Differential expression levels of PLOD2 in the GSE16573 and TCGA-KIRC cohorts. (C) Hazard ratios of PLOD2 in different ccRCC cohorts. (D) Differential proliferation abilities of OSRC2 and 786-O cells in the NC group and PLOD2 knockdown (sh-PLOD2) group. (E, F) Wound healing assay and Transwell experiments demonstrate the migration and invasion abilities of OSRC2 and 786-O cells. NC, normal control; OS, overall survival; PFI, progression-free interval.

SEMA3, HSPG, EPHA, NECTIN, TIGIT, SEMA6, SELPLG, AGRN and *IFG* (Fig. 6G).

3.7. PLOD2 promotes ccRCC progression by modulating the cell cycle and genome instability

Among the 12 genes in the TDERS, we noticed that PLOD2 was a risk factor for both OS and recurrence-free interval (RFI) in ccRCC when perform Univariate Cox analysis (Fig. 7A). Compared with normal tissues from GSE167573 and TCGA-KIRC, PLOD2 was significantly overexpressed in tumor tissues (Fig. 7B). The expression level of PLOD2 was higher in patients with advanced clinical stage and grade across different cohorts (Supplementary Fig. 9A). Univariate Cox analysis further revealed that a high expression level of PLOD2 indicated worse progression in terms of OS, DFS and PFS in ccRCC (Fig. 7C). Interestingly, we noticed that patients divided into PLOD2 high-expression groups had a frequent mutation rate of KDM5C and SPEN, which suggested that two epigenetic factors might be involved in the transcriptional regulation of PLOD2 in ccRCC (Supplementary Fig. 9B). PLOD2 might regulate protein hydroxylation, RNA degradation, DNA mismatch, E2F, and the G2M checkpoint in ccRCC (Supplementary Fig. 9C-E). In addition, we applied siRNA against PLOD2 and transfected it into two common ccRCC cell lines, OSRC2 and 786-0. RT-PCR and western blotting showed satisfactory know-down efficacy of PLOD2 in ccRCC cell line (Supplementary Fig. 10A). CCK8, wound healing, migration and invasion experiments showed that ccRCC cell lines treated with PLOD2 siRNA exhibited hampered cell proliferation and migration (Fig. 7D–F). Besides, dysregulated

expression level of PLOD2 has tumor-promoter effect in other RCC histology types including KIRP and KICH. In detail, high expression level of PLOD2 was correlated with short survival time in TCGA-KIRC, KIRP and KICH (Supplementary Fig. 10B-D).

4. Discussion

The complexity of histopathological diagnosis for RCC is further compounded by the inclusion of additional histological subtypes with distinct molecular features in the World Health Organization (WHO) classification, such as clear cell papillary RCC, as well as the frequent occurrence of heterogeneous mixed-histological tumors and intratumoral heterogeneity (ITH).[34] It is imperative to emphasize the necessity for a universally applicable risk assessment system. Thus, we also evaluated the prognosis predictive ability of TDERS in three RCC pathology types, including ccRCC, pRCC and chRCC. Surprisingly, TEDRS has demonstrated superior accuracy in forecasting OS at the 5-year milestone when juxtaposed with the existing TNM staging system, specifically for the aforementioned three pathological types. Additionally, we conducted an analysis to determine the root cause of the difference between the high and low TDERS groups. The results showed a positive correlation between the high-risk group and multiple oncogenic pathways, including KRAS, hypoxia, myogenesis, peroxisome, and coagulation. Furthermore, the high-risk group demonstrated a lower mutational burden, which may result in a weaker response to immunotherapy. To address this, we explored molecular inhibitors that could potentially be effective in treating drug-refractory high-risk groups, such as LFM.

A13 and RO.3306, which act as direct inhibitors of the BTK and CDK1 pathways, respectively. These inhibitors present promising therapeutic targets for the TDERS high group among RCC patients.

In terms of prognosis, a prognostic model based on genome-related signatures can offer additional predictive value to the current staging system, allowing for more precise prediction of cancer prognosis.[35] For instance, the 21-gene recurrence score can classify breast cancer patients with the same clinical stage into low-risk and high-risk subgroups.[36] This classification reveals significant differences in RFI and aids clinicians in making decisions regarding adjuvant therapy. Patients identified as high-risk based on the 21-gene recurrence score may benefit from adjuvant therapy due to their increased recurrence rate. On the other hand, identifying low-risk patients in the same clinical stage can prevent unnecessary overtreatment, particularly when the benefits of adjuvant therapy are minimal compared to surgery alone. In the case of localized ccRCC, the six single nucleotide polymorphism (SNP)-based score and the 16-gene assay offer a more accurate assessment of recurrence risk beyond the existing staging systems.[37] Moreover, our risk model system was developed based on dysregulated signatures found in exosomes derived from the plasma of ccRCC patients. This targeted dysregulation offers advantages such as easy sample availability, non-invasive examination, and tumor specificity. Additionally, our work has uncovered some interesting findings. We observed that patients with a high TDERS exhibited activation of pathways related to cornification, hypoxia, coagulation, and the inflammatory response while displaying a constrained state of heme metabolism, tumor antigen presentation, and monocyte recruitment. These clues indicate that aberrant coagulation in the TDERS group may hinder the anti-immune process and promote cancer progression. It is worth noting that the coagulation system, particularly the tissue factor (TF) pathway, plays a vital role in innate defence mechanisms, such as stopping bleeding, limiting infection, and aiding wound repair.[38] Tumor cells often exploit these host protective pathways to shape the TME and facilitate metastasis. In the context of metastasis, TF-initiated coagulation, fibrinogen, and PAR4 signaling activate platelets, which in turn support tumor cell survival in the bloodstream and their settlement at distant sites.[39] Interestingly, Queiroz et al. found that the growth of PAR1-deficient pancreatic cancer cells could be restored by depleting tumor-eradicating cytotoxic CD8$^+$ T cells, suggesting the involvement of tumor cell PAR1 signalling in preventing immune surveillance and contributing to immune evasion by primary tumors.[40] Interestingly, we first noticed that cornification might promote RCC progression in TDERS high group. A work from Qin et al. found cornification related protein, Peptidylargininedeiminase 1 or PAD1, could promote tumorigenesis by regulating MEK1-ERK1/2-MMP2 signaling in triple negative breast cancer.[41] Another work from Fiskin revealed disrupted cornification could induce immune dysfunction state in human skin, which were consistent with our finding that TDERS high group with cornification activated state resulted with immune dysfunction.[42] We also observed that the increased hypoxic state in the high TDERS group could interact with macrophages in the tumor, thus facilitating the progression of ccRCC, which is consistent with previous studies. Hypoxia is a critical factor that affects the communication between tumor cells and tumor-associated macrophages (TAM).[43] Hypoxia influences the crosstalk between TAMs and tumor cells through various mechanisms, including the release of multifunctional exosomes, cytokines, growth factors, cellular debris, oncometabolites, and the interaction of ligands and receptors on the cell surface. The hypoxia-induced interaction between tumor cells and TAMs promotes tumor proliferation, migration, invasion, angiogenesis, drug resistance, epithelial–mesenchymal transition (EMT), and cancer stem cell self-renewal. Additionally, hypoxia also promotes macrophage phagocytosis, which inhibits tumor cell proliferation. Exosomes released from hypoxic epithelial ovarian cancer cells deliver miR-21–3p, miR-125b-5p, and miR-181d-5p to macrophages, inducing M2 macrophage polarization and ultimately leading to tumor proliferation and migration.[44,45] Tumor-derived exosomal HMMR-AS1 also regulates M2-shifted polarization through the miR147a/ARID3A axis.[46]

Considering the increased expression of PLOD2 as a characteristic of patients with high TDERS scores, targeting PLOD2 may restore the innate TME of ccRCC and enhance the efficacy of ICIs in the high TDERS group. Interestingly, our study unveils that PLOD2 emerges as the sole molecule upregulated in the cohort with high TDERS, underscoring its paramount significance in driving the progression of renal carcinoma (Supplementary Fig. 2A). Through differential analysis between groups with high and low scores, we discerned that pathway including KRAS, hypoxia, myogenesis, peroxisome, and coagulation are notably activated in the high-risk group, suggesting these pathways might serve as either upstream or downstream conduits influenced by aberrant PLOD2 expression. Concurrently, previous research has illuminated that PLOD2 can engage in crosstalk with the aforementioned pathways or signaling axes, thereby facilitating tumor progression. A previous work discovered a tumor-specific splicing variant of macrophage receptor with collagenous structure-TST (MARCO-TST), which could interacted with PLOD2 and enhanced the stability of HIF-1α, resulting the metabolic dysregulation of triple-negative breast cancer and forming a hypoxic tumor microenvironment.[47] Daniel and colleagues demonstrated that mechanical (stress relaxation) and chemical (hypoxia) properties of the tumor microenvironment jointly accelerate sarcoma motility and metastasis via increased expression of collagen matrix crosslinker PLOD2. These investigations accentuate the pivotal role of PLOD2 in modulating tumor progression through its engagement with the collagen pathway and the hypoxic microenvironment.

Recent investigations have further delineated the pivotal role of PLOD2 in promoting malignant phenotypes across various cancers. Studies by Tong et al. revealed that in breast cancer EMT, PLOD2 is associated with increased cytoplasmic succinate, driving mesenchymal transformations and enhancing cancer cell stemness while reducing 5-hydroxymethylcytosine (5hmC) levels in chromatin upon silencing of PLOD2.[48] Additionally, Lan et al. uncovered a critical interaction between PLOD2 and USP15, a deubiquitinating enzyme, that stabilizes and activates the AKT/mTOR signaling pathway, consequently fostering the progression of colorectal cancer.[49] This interaction underscores the emerging complexities of PLOD2's role in cancer signaling networks. Furthermore, using data-independent acquisition mass spectrometry (DIA-MS) analyses of formalin-fixed paraffin-embedded (FFPE) tissue samples, Shao et al. posited PLOD2 as a novel therapeutic target in colorectal cancer, linking its expression with disease progression and potential poor prognosis.[50] Notably, previous research in RCC has also highlighted the significance of PLOD2 at the proteomics level. RNA sequencing and proteomic studies in East Asian populations have shown that PLOD2 could serve as a novel biomarker in ccRCC due to its medium to strong tumor-specific staining in more than 90% of samples.[51] Additionally, Klatt et al. found that PLOD2 could function as a tumor-associated antigen and elicit a T-cell response.[52] In addition, previous works have indicated the role of PLOD2 in the progression of ccRCC. Liu et al. found deregulated expression level of PLOD2 was partially mediated by hypoxia related transcriptome factor, HIF1A, in ccRCC, which interacted with EGFR and led disrupted phosphorylation of EGFR, ultimately activating the AKT signalling.[53] Furthermore, Chen and colleagues proposed that under prolonged hypoxia, the HIF/METTL3/PLOD2 axis could serve as a biomarker for RCC prognosis.[54] Collectively, these studies not only reinforce PLOD2's centrality in cancer biology but also highlight its potential as a target for therapeutic intervention, especially in ccRCC.

In our study, we demonstrated that inhibiting PLOD2 significantly reduced the invasion and migration capacity of ccRCC cell lines. Computational analysis suggested that dysregulated PLOD2 expression in ccRCC could impact protein processing and DNA replication, affecting tumor antigen presentation and ICI response. We also observed higher expression of PLOD2 in cancer cells at the single-cell level and found that high TDERS scores hindered macrophage infiltration in ccRCC. It is essential to further investigate whether PLOD2 influences immune invasion and metabolic reprogramming. Moreover, our model performed well in two

other pathological types of RCC, demonstrating internal consistency and suggesting potential relevance beyond ccRCC.

To the best of our knowledge, our study is the first to include a sample size larger than 2000 in the context of RCC, and the findings also hold relevance for patients with pRCC and chRCC. Furthermore, our risk score system demonstrated impressive performance within ICI cohorts. We employed two well-established approaches to validate the effectiveness of our risk scoring system, including model detection, validation, and assessment using external datasets. These approaches have successfully demonstrated the accuracy and specificity of TDERS. Nevertheless, it is crucial to recognize the constraints faced in our research, which must be considered in future inquiries. The retrospective nature of all cohorts examined in our study underscores the necessity for additional validation via prospective studies carried out in a multicenter environment. Furthermore, the intricate biological functions of particular mRNA molecules within TDERS, such as PLOD2, were exclusively analyzed through computational techniques. Subsequent investigations should incorporate *in vivo* and *in vitro* experiments to comprehensively comprehend their roles in RCC.

5. Conclusions

To summarize, our risk stratification scoring system utilizes signatures from exosomes, making it a pragmatic and dependable prognostic instrument for patients diagnosed with ccRCC, kidney renal papillary cell carcinoma (pRCC) and kidney chromophobe carcinoma (chRCC). This system acts as a valuable supplement to the current staging system by accurately predicting the overall survival duration following surgical intervention. By efficiently identifying RCC patients who are at either high or low risk of postsurgical recurrence, our assay aids in making well-informed treatment decisions and facilitates the exploration of adjuvant therapy through clinical trials.

In conclusion, our risk stratification scoring system incorporates exosome signatures to provide a practical and reliable prognostic tool for patients with ccRCC, pRCC, and chRCC. This system serves as a valuable adjunct to the existing staging system by accurately forecasting postsurgical overall survival duration. By effectively distinguishing RCC patients at high or low risk of recurrence after surgery, our assay assists in guiding informed treatment decisions and enables the investigation of adjuvant therapy in clinical trials.

Declaration of competing interest

The authors declare that they have no known competing financial interests or personal relationships that could have appeared to influence the work reported in this paper.

Ethical statement

All of the study designs and test procedures were performed in accordance with the Helsinki Declaration II. The ethics approval and participation consent of this study was approved by the ethics committee of Changhai Hospital (Ethical number: CHEC2021-091). All patients participating in this study signed informed consent forms.

Data availability

The original contributions presented in the study are summarized in the Methods and Materials section, and further questions can be addressed to the corresponding authors. Any additional information required to reanalyze the data reported in this paper is available from the correspondence authors upon request.

Acknowledgments

Author contributions

L.W., P.L., W.X., L.Q. and X.G. conducted the conception and design and administrated the support. A.J., Y.L., Z.H., W.L. and Q.Y. performed provision of study materials, collection and assembly of data, data analysis and wet experiment. A.J. and Y.L. conducted graphs plotting. Y.F., B.Z. and X.W. provided suggestions for revisions. All of the authors drafted and revised this manuscript.

Supplementary materials

Supplementary material associated with this article can be found, in the online version, at doi:10.1016/j.jncc.2024.07.002.

References

1. Powles T, Albiges L, Staehler M, et al. Updated European association of urology guidelines: recommendations for the treatment of first-line metastatic clear cell renal cancer. *Eur Urol.* 2018;73:311–315.
2. Siegel RL, Miller KD, Fuchs HE, Jemal A. Cancer statistics, 2022. *CA Cancer J Clin.* 2022;72:7–33.
3. Han B, Zheng R, Zeng H, et al. Cancer incidence and mortality in China, 2022. *J Natl Cancer Cent.* 2024;4:47–53.
4. Stewart SB, Thompson RH, Psutka SP, et al. Evaluation of the national comprehensive cancer network and American urological association renal cell carcinoma surveillance guidelines. *J Clin Oncol.* 2014;32:4059–4065.
5. Motzer RJ, Jonasch E, Agarwal N, et al. Kidney cancer, Version 3.2022, NCCN clinical practice guidelines in oncology. *J Natl Compr Canc Netw.* 2022;20:71–90.
6. Choueiri TK, Tomczak P, Park SH, et al. Adjuvant pembrolizumab after nephrectomy in renal-cell carcinoma. *N Engl J Med.* 2021;385:683–694.
7. Ravaud A, Motzer RJ, Pandha HS, et al. Adjuvant sunitinib in high-risk renal-cell carcinoma after nephrectomy. *N Engl J Med.* 2016;375:2246–2254.
8. Zhou M, He X, Mei C, Ou C. Exosome derived from tumor-associated macrophages: biogenesis, functions, and therapeutic implications in human cancers. *Biomark Res.* 2023;11:100.
9. Qi R, Bai Y, Li K, et al. Cancer-associated fibroblasts suppress ferroptosis and induce gemcitabine resistance in pancreatic cancer cells by secreting exosome-derived ACSL4-targeting miRNAs. *Drug Resist Updat.* 2023;68:100960.
10. Li Y, Zhao W, Wang Y, Wang H, Liu S. Extracellular vesicle-mediated crosstalk between pancreatic cancer and stromal cells in the tumor microenvironment. *J Nanobiotechnol.* 2022;20:208.
11. Guo X, Gao C, Yang D-H, Li S. Exosomal circular RNAs: a chief culprit in cancer chemotherapy resistance. *Drug Resist Updat.* 2023;67:100937.
12. Ye H, Hu X, Wen Y, et al. Exosomes in the tumor microenvironment of sarcoma: from biological functions to clinical applications. *J Nanobiotechnol.* 2022;20:403.
13. Asleh K, Dery V, Taylor C, Davey M, Djeungoue-Petga M-A, Ouellette RJ. Extracellular vesicle-based liquid biopsy biomarkers and their application in precision immuno-oncology. *Biomark Res.* 2023;11:99.
14. Nawaz M, Camussi G, Valadi H, et al. The emerging role of extracellular vesicles as biomarkers for urogenital cancers. *Nat Rev Urol.* 2014;11:688–701.
15. Qu L, Ding J, Chen C, et al. Exosome-transmitted lncARSR promotes sunitinib resistance in renal cancer by acting as a competing endogenous RNA. *Cancer Cell.* 2016;29:653–668.
16. Motzer RJ, Banchereau R, Hamidi H, et al. Molecular subsets in renal cancer determine outcome to checkpoint and angiogenesis blockade. *Cancer Cell.* 2020;38:803–817.
17. Braun DA, Hou Y, Bakouny Z, et al. Interplay of somatic alterations and immune infiltration modulates response to PD-1 blockade in advanced clear cell renal cell carcinoma. *Nat Med.* 2020;26:909–918.
18. Blum A, Wang P, Zenklusen JC. SnapShot: tCGA-analyzed tumors. *Cell.* 2018;173:530. https://www.sciencedirect.com/science/article/pii/S009286741830391X.
19. Barrett T, Wilhite SE, Ledoux P, et al. NCBI GEO: archive for functional genomics data sets–update. *Nucleic Acids Res.* 2013;41:D991–D995.
20. Love MI, Huber W, Anders S. Moderated estimation of fold change and dispersion for RNA-seq data with DESeq2. *Genome Biol.* 2014;15:550.
21. Yu G, Wang L-G, Han Y, He Q-Y. clusterProfiler: an R package for comparing biological themes among gene clusters. *OMICS.* 2012;16(5):284–287.

22. Liberzon A, Subramanian A, Pinchback R, Thorvaldsdóttir H, Tamayo P, Mesirov JP. Molecular signatures database (MSigDB) 3.0. *Bioinformatics*. 2011;27:1739–1740.

23. Mayakonda A, Lin DC, Assenov Y, Plass C, Koeffler HP. Maftools: efficient and comprehensive analysis of somatic variants in cancer. *Genome Res*. 2018;28:1747–1756.

24. Charoentong P, Finotello F, Angelova M, et al. Pan-cancer immunogenomic analyses reveal genotype-immunophenotype relationships and predictors of response to checkpoint blockade. *Cell Rep*. 2017;18:248–262.

25. Mermel CH, Schumacher SE, Hill B, Meyerson ML, Beroukhim R, Getz G. GISTIC2.0 facilitates sensitive and confident localization of the targets of focal somatic copy-number alteration in human cancers. *Genome Biol*. 2011;12:R41.

26. Jiang P, Gu S, Pan D, et al. Signatures of T cell dysfunction and exclusion predict cancer immunotherapy response. *Nat Med*. 2018;24:1550–1558.

27. Jiang A, Meng J, Gong W, et al. Elevated SNRPA1, as a promising predictor reflecting severe clinical outcome via effecting tumor immunity for ccRCC, is related to cell invasion, metastasis, and sunitinib sensitivity. *Front Immunol*. 2022;13:842069. https://www.frontiersin.org/article/10.3389/fimmu.2022.842069.

28. Jiang A, Meng J, Bao Y, et al. Establishment of a prognosis prediction model based on pyroptosis-related signatures associated with the immune microenvironment and molecular heterogeneity in clear cell renal cell carcinoma. *Front Oncol*. 2021;11:755212. https://www.frontiersin.org/article/10.3389/fonc.2021.755212.

29. Jiang A, Luo P, Chen M, et al. A new thinking: deciphering the aberrance and clinical implication of copper-death signatures in clear cell renal cell carcinoma. *Cell Biosci*. 2022;12:209.

30. Jiang A, Xu Z, Fang X, et al. RNA modification pattern-based subtypes reveal heterogenous clinical outcomes and tumor immunity of clear cell renal cell carcinoma. *MedComm*. 2023;2:e30. https://onlinelibrary.wiley.com/doi/10.1002/mef2.30.

31. Kurokawa M, Naito S, Kato T, et al. Complete response to an anti-programmed cell death 1 antibody following a combination therapy of an anti-programmed cell death ligand 1 antibody and a tyrosine kinase inhibitor for metastatic renal cell carcinoma. *Asian J Urol*. 2023;10:103–105. https://www.sciencedirect.com/science/article/pii/S2214388222000509.

32. Roh W, Chen PL, Reuben A, et al. Integrated molecular analysis of tumor biopsies on sequential CTLA-4 and PD-1 blockade reveals markers of response and resistance. *Sci Transl Med*. 2017;9:eaah3560.

33. Sia D, Jiao Y, Martinez-Quetglas I, et al. Identification of an immune-specific class of hepatocellular carcinoma, based on molecular features. *Gastroenterology*. 2017;153:812–826.

34. Büttner FA, Winter S, Stühler V, et al. A novel molecular signature identifies mixed subtypes in renal cell carcinoma with poor prognosis and independent response to immunotherapy. *Genome Med*. 2022;14:105.

35. Qu L, Wang ZL, Chen Q, et al. Prognostic value of a long non-coding RNA signature in localized clear cell renal cell carcinoma. *Eur Urol*. 2018;74:756–763.

36. Albain KS, Barlow WE, Shak S, et al. Prognostic and predictive value of the 21-gene recurrence score assay in postmenopausal women with node-positive, oestrogen-receptor-positive breast cancer on chemotherapy: a retrospective analysis of a randomised trial. *Lancet Oncol*. 2010;11:55–65.

37. Wei JH, Feng ZH, Cao Y, et al. Predictive value of single-nucleotide polymorphism signature for recurrence in localised renal cell carcinoma: a retrospective analysis and multicentre validation study. *Lancet Oncol*. 2019;20:591–600.

38. Ruf W, Graf C. Coagulation signaling and cancer immunotherapy. *Thromb Res*. 2020;191:S106–S111.

39. Magnus N, Garnier D, Rak J. Oncogenic epidermal growth factor receptor up-regulates multiple elements of the tissue factor signaling pathway in human glioma cells. *Blood*. 2010;116:815–818.

40. Queiroz KCS, Shi K, Duitman J, et al. Protease-activated receptor-1 drives pancreatic cancer progression and chemoresistance. *Int J Cancer*. 2014;135:2294–2304.

41. Qin H, Liu X, Li F, et al. PAD1 promotes epithelial-mesenchymal transition and metastasis in triple-negative breast cancer cells by regulating MEK1-ERK1/2-MMP2 signaling. *Cancer Lett*. 2017;409:30–41.

42. Fiskin E., Eraslan G., Alora-Palli M.B., et al. Multi-modal skin atlas identifies a multicellular immune-stromal community associated with altered cornification and specific T cell expansion in atopic dermatitis. bioRxiv [Preprint]. 2023:2023.10.29.563503.

43. Bai R, Li Y, Jian L, Yang Y, Zhao L, Wei M. The hypoxia-driven crosstalk between tumor and tumor-associated macrophages: mechanisms and clinical treatment strategies. *Mol Cancer*. 2022;21:177.

44. Wang X, Luo G, Zhang K, et al. Hypoxic tumor-derived exosomal miR-301a mediates M2 macrophage polarization via PTEN/PI3Kγ to promote pancreatic cancer metastasis. *Cancer Res*. 2018;78:4586–4598.

45. Zhu X, Shen H, Yin X, et al. Macrophages derived exosomes deliver miR-223 to epithelial ovarian cancer cells to elicit a chemoresistant phenotype. *J Exp Clin Cancer Res*. 2019;38:81.

46. Wang X, Zhou Y, Dong K, Zhang H, Gong J, Wang S. Exosomal lncRNA HMMR-AS1 mediates macrophage polarization through miR-147a/ARID3A axis under hypoxia and affects the progression of hepatocellular carcinoma. *Environ Toxicol*. 2022;37:1357–1372.

47. Lewis DM, Pruitt H, Jain N, et al. A feedback loop between hypoxia and matrix stress relaxation increases oxygen-axis migration and metastasis in sarcoma. *Cancer Res*. 2019;79:1981–1995.

48. Tong Y, Qi Y, Xiong G, et al. The PLOD2/succinate axis regulates the epithelial-mesenchymal plasticity and cancer cell stemness. *Proc Natl Acad Sci USA*. 2023;120:e2214942120.

49. Lan J, Zhang S, Zheng L, et al. PLOD2 promotes colorectal cancer progression by stabilizing USP15 to activate the AKT/mTOR signaling pathway. *Cancer Sci*. 2023;114:3190–3202.

50. Shao Y, Xu K, Zheng X, et al. Proteomics profiling of colorectal cancer progression identifies PLOD2 as a potential therapeutic target. *Cancer Commun (Lond)*. 2022;42:164–169.

51. Qu Y, Feng J, Wu X, et al. A proteogenomic analysis of clear cell renal cell carcinoma in a Chinese population. *Nat Commun*. 2022;13:2052. https://www.nature.com/articles/s41467-022-29577-x.

52. Klatt MG, Kowalewski DJ, Schuster H, et al. Carcinogenesis of renal cell carcinoma reflected in HLA ligands: a novel approach for synergistic peptide vaccination design. *Oncoimmunology*. 2016;5:e1204504.

53. Liu T, Xiang W, Chen Z, et al. Hypoxia-induced PLOD2 promotes clear cell renal cell carcinoma progression via modulating EGFR-dependent AKT pathway activation. *Cell Death Dis*. 2023;14:774.

54. Chen Y, He Y, Li Z, et al. METTL3 facilitates renal cell carcinoma progression by PLOD2 m6A-methylation under prolonged hypoxia. *Cell Death Dis*. 2024;15:62.